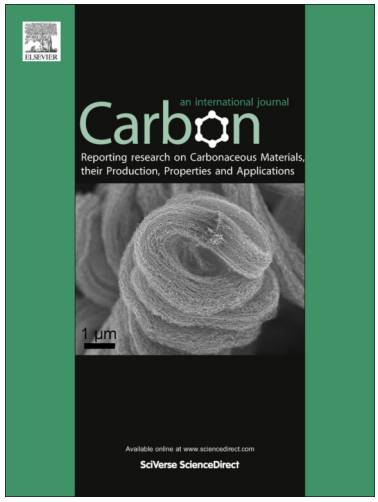

Dense carbon monoliths for supercapacitors with outstanding volumetric capacitances

M. Kunowsky, A. Garcia-Gomez, V. Barranco, J.M. Rojo, J. Ibañez, J.D. Carruthers, A. Linares-Solano

PII: S0008-6223(13)01094-4
DOI: http://dx.doi.org/10.1016/j.carbon.2013.11.034
Reference: CARBON 8545

To appear in: *Carbon*

Received Date: 5 September 2013
Accepted Date: 14 November 2013

Please cite this article as: Kunowsky, M., Garcia-Gomez, A., Barranco, V., Rojo, J.M., Ibañez, J., Carruthers, J.D., Linares-Solano, A., Dense carbon monoliths for supercapacitors with outstanding volumetric capacitances, *Carbon* (2013), doi: http://dx.doi.org/10.1016/j.carbon.2013.11.034

Dense carbon monoliths for supercapacitors with outstanding volumetric capacitances

M. Kunowsky[a], A. Garcia-Gomez[b], V. Barranco[b], J.M. Rojo[b], J. Ibañez[c], J.D. Carruthers[d], A. Linares-Solano[a*]

[a] Grupo de Materiales Carbonosos y Medio Ambiente, Departamento de Química Inorgánica, Universidad de Alicante, Ap. 99, E-03080 Alicante, Spain.

[b] Instituto de Ciencia de Materiales de Madrid (ICMM), CSIC; Sor Juana Inés de la Cruz, 3; Cantoblanco; 28049 Madrid, Spain.

[c] Centro Nacional de Investigaciones Metalurgicas (CENIM), CSIC; Avenida Gregorio del Amo, 8; 28040 Madrid, Spain.

[d] ATMI, Adsorbent & Gas Technology, Danbury, Connecticut 06810, USA.

[*] *Corresponding autor:* E-mail: linares@ua.es;
Tel: +34 965 90 35 45; Fax: +34 965 90 34 54.

Abstract

A commercially available dense carbon monolith (CM) and four carbon monoliths obtained from it have been studied as electrochemical capacitor electrodes in a two-electrode cell. CM has: i) very high density (1.17 g cm^{-3}), ii) high electrical conductivity (9.3 S cm^{-1}), iii) well-compacted and interconnected carbon spheres, iv) homogeneous microporous structure and v) apparent BET surface area of 957 m^2g^{-1}. It presents interesting electrochemical behaviors (*e.g.*, excellent gravimetric capacitance and outstanding volumetric capacitance). The textural characteristics of CM (porosity and surface chemistry) have been modified by means of different treatments. The electrochemical performances of the starting and treated monoliths have been analyzed as a function of their porous textures and surface chemistry, both on gravimetric and volumetric basis. The monoliths present high specific and volumetric capacitances (292 F g^{-1} and 342 F cm^{-3}), high energy densities (38 Wh kg^{-1} and 44 Wh L^{-1}), and high power densities (176 W kg^{-1} and 183 W L^{-1}). The specific and volumetric capacitances, especially the volumetric capacitance, are the highest ever reported for carbon monoliths. The high values are achieved due to a suitable combination of density, electrical conductivity, porosity and oxygen surface content.

1. Introduction

Electrochemical capacitors, also called supercapacitors or ultracapacitors, are energy storage devices with interesting properties (*e.g.*, short discharge times, high power densities and long cycle life) that are useful for a large number of applications [1-5]. Because their main drawback is the low energy density, today´s intense research efforts continue to improve this property [3-5]. Thus, new types of carbon electrodes are being tested (*e.g.*, carbon monoliths [4,6-15]) and new attempts, to further increase and control their porosity (pore size distributions and surface chemistry) are going on [4,7-9,13,16-19]. Another challenge is to scale up production, in order to provide more favorable economical feasibility [20,21].

Carbon monoliths consist of a three-dimensional network of linked carbon particles, having well connected micro-, meso- and macroporosity [16,22-26]. This characteristic has led to some useful applications of carbon monoliths for gas storage systems. For example, for on-board fuel storage (*i.e.*, of H_2 and CH_4) [27,28] or for safe transportation (*e.g.*, of volatile organic compound, carbon dioxide or dangerous compounds) [28-30]. Moreover, carbon monoliths show high electrical conductivity, which comes from the easy movement of charge carriers within individual carbon particles and through the border of adjacent particles. Compared to compacted powder pellets monoliths show higher electrical conductivity, which results from the better contact between adjacent particles [10]. Both characteristics, network porosity and electrical conductivity, account for the application of carbon monoliths as supercapacitor electrodes.

Although carbon monoliths have been prepared for long time [15,16,22-26,31-38], *e.g.*, as carbon aerogels or xerogels, only in the last 3-4 years they have been studied as electrodes in their current form, *i.e.,* as an entire piece of carbon [8-14,17,18,23,39-43]. Cells of supercapacitors made of carbon monoliths as electrodes have a number of advantages over those made of compacted powder pellets. They reach higher capacitances, lower resistances and shorter response times (*i.e.*, faster charge/discharge of the cell) [10]. The three-dimensional character of a monolith causes that its thickness affects the electrical response of the cell. Longer monoliths are better for improving the cell energy and shorter monoliths are better for improving the cell power [40,41].

The main drawback of carbon monoliths is their low density (typically less than 0.5-0.6 g cm^{-3}) which leads to low volumetric capacitances (usually less than 100-150 F cm^{-}

^{3} in aqueous electrolytes and less than 50-100 F cm^{-3} in organic ones) [4,8,9-11,14,22-26,40-43].

The present study reports the electrochemical performances (*i.e.*, capacitances, power densities and energy densities) of a commercial dense carbon monolith [28,29,44] and of four additional monoliths prepared from it. The results are discussed on both, gravimetric and volumetric basis. Oftentimes, the electrode performances are reported only on gravimetric basis, *i.e.*, the usually called specific capacitance, but results expressed on volumetric basis are more important from an application point of view [21]. The starting monolith presents excellent performances *e.g.*, high gravimetric and outstanding volumetric capacitances. In order to delve into the understanding of this exceptional behavior, four modified monoliths have also been studied. One monolith (CM-N_2) was obtained by heat-treatment of the starting monolith CM in a N_2 flow at 1073 K, to change the surface chemistry, while preserving the surface characteristics (surface area and porosity). Another monolith (CM-Ar) was obtained by heat-treatment of the starting CM monolith in an Ar flow at 2273 K to strongly modify both, surface chemistry and porosity. Two other monoliths were obtained by heat-treatment in a N_2 flow at 1073 K, similar to CM-N_2, followed by subsequent activation at this temperature in CO_2 flow during 24 h or 48 h (CM-24 and CM-48), the activation treatment allowing the change of the surface chemistry and surface characteristics at the same time. The densities and electrical conductivities of the monoliths are measured and discussed on the basis of the applied treatments.

2. Materials and methods

The starting carbon monolith was produced by ATMI Adsorbent & Gas Technology from pyrolysis of a PVDC (polyvinylidene chloride) copolymer [28,29,44]. It is commercially available with a cylindrical shape of 9 cm in diameter and 2 cm in height (BrightBlack^{TM}, ATMI Adsorbent & Gas Technology), as it is shown on the left hand side in Figure 1a. From it, smaller cylindrical monoliths were cut out, having 10 mm in diameter and 16 mm in height (see Figure 1a, middle). These monoliths (CM) were used to prepare two heat-treated monoliths (CM-N_2 and CM-Ar) and the two activated monoliths (CM-24 and CM-48).

i) CM-N_2: This monolith was obtained by heat-treatment of CM under N_2 flow (100 ml min^{-1}) at 1073 K for 3 h. The heating rate was 5 K min^{-1}. For cooling, the furnace was switched off and allowed to cool down to room temperature by convection. The N_2 flow

was also applied during the cooling run.

ii) CM-Ar: This monolith was obtained by heating CM under Ar flow (100 ml min^{-1}) at 2273 K for 1 h. The heating run was under Ar flow at 5 K min^{-1}. The cooling to room temperature by convection was also performed under Ar flow.

iii) CM-24 and CM-48: These monoliths were obtained from CM according to the following treatments: Firstly, the monolith was heated, as CM-N_2, from room temperature up to 1073 K under N_2 flow (100 ml min^{-1}). Once that temperature was reached, the N_2 flow was changed to CO_2 (100 ml min^{-1}), keeping the temperature at 1073 K either for 24 h (CM-24) or for 48 h (CM-48). Once the activation time was over, the CO_2 flow was again changed to N_2, and the furnace was cooled down to room temperature by convection.

The microstructural characterization was carried out by scanning electron microscopy (SEM) in a Jeol JSM 6500 F instrument, using the secondary electron mode. In a particular case (Figure 1d), the SEM images were obtained on the monolith embedded in a resin, which was cured and then polished.

Sub-atmospheric N_2 (at 77 K) and CO_2 (at 273 K) adsorption/desorption isotherms were measured in a Micromeritics ASAP 2020. Previous to the experiments, the samples were outgassed under vacuum at 523 K for at least 5 h. The Dubinin-Raduskevich equation was applied to both, N_2 and CO_2 adsorption isotherms, to calculate the micropore volumes, V_{DR}. While from N_2 adsorption data the total micropore volume ($V_{DR}(N_2)$) was obtained, CO_2 adsorption data takes into account only the narrow micropore volumes ($V_{DR}(CO_2)$), *i.e.,* the volume adsorbed in micropores < 0.7 nm. From the N_2 adsorption isotherms, the apparent BET (Brunauer-Emmett-Teller) surface areas (S_{BET}) were calculated (in the range from 0.001 to 0.1 P/P_o). Additionally, from non-local density functional theory (NLDFT) the pore size distributions (PSD) were obtained. In addition to S_{BET}, other apparent surface areas have been assessed from the N_2 adsorption data using the most frequently used methods, *i.e.*, α-plot ($S_{\alpha\text{-plot}}$, using the CM-Ar sample as reference), t-method ($S_{t\text{-plot}}$), Dubinin-Raduskevich (S_{DR}), and NLDFT (S_{DFT}, taking into account pores smaller than 2 nm). The latter two methods have also been applied to CO_2 adsorption data.

The densities of the monoliths were determined at room temperature from the weight and volume of the degassed monoliths. The volume was determined from the monolith geometric dimensions, which are easily measurable due to the cylindrical shape.

Temperature-programmed desorption (TPD) measurements were performed in a

thermogravimetric device (SDT Q600, TA Instruments), coupled to a mass spectrometer (Thermostar GSD 300 T3, Balzers Instruments). A heating rate of 10 K min^{-1} was used, and the maximum temperature of 1173 K was maintained constant for 30 min. The experiments were carried out under a He flow of 100 ml min^{-1}. The evolved CO and CO_2 groups have been quantified by using calcium oxalate as a reference material.

The cylindrical monoliths, of 10 mm in diameter and 16 mm in height, were cut in slices of the same diameter and 1.3-1.6 mm in height (see the right hand side in Figure 1a). These smaller monoliths were used as electrodes in two- and three-electrode cells. For the measurements in the former cell, two equal carbon monoliths were separated by a glassy microfiber paper (Whatman 934 AH). In the three-electrode cell (used to check the presence of pseudocapacitance by cyclic voltammetry), the carbon monolith acted as the working electrode, Hg/Hg_2SO_4 as the reference electrode, and platinum wire as the counter electrode. In the two types of cells, 2M H_2SO_4 aqueous solution was chosen as the electrolyte solution. Previous to the electrochemical measurements, the monoliths were infiltrated with the electrolyte solution under a vacuum of $1.3*10^{-6}$ MPa for 1.5 days.

The electrical conductivity of the monoliths was determined by the four-probe method. The cylindrical monoliths were transformed into parallelepipedic pieces by polishing the former. The parallelepipedic pieces had dimensions of 9x8x1 mm^3. A commercial silver paint was chosen to get the four probes.

3. Results and discussion

3.1. Microstructure, density, electrical conductivity and surface oxygen content

SEM images of the starting monolith CM show a carbon material formed by spheres, which are made from interconnected particles (Figures 1b and c). The spheres have diameters around 200 µm (Figure 1b). The individual particles have sizes of ca. 10 µm (Figure 1c). The spheres are interconnected through adjacent particles (Figure 1b and d). Between adjacent spheres (Figure 1b) and adjacent particles (Figure 1c) appear voids of micrometer size, 40 µm-size in the former case and 4 µm-size in the latter. Moreover, the two types of voids are interconnected along the monolith bulk allowing an ease access of the electrolyte to the carbon particles.

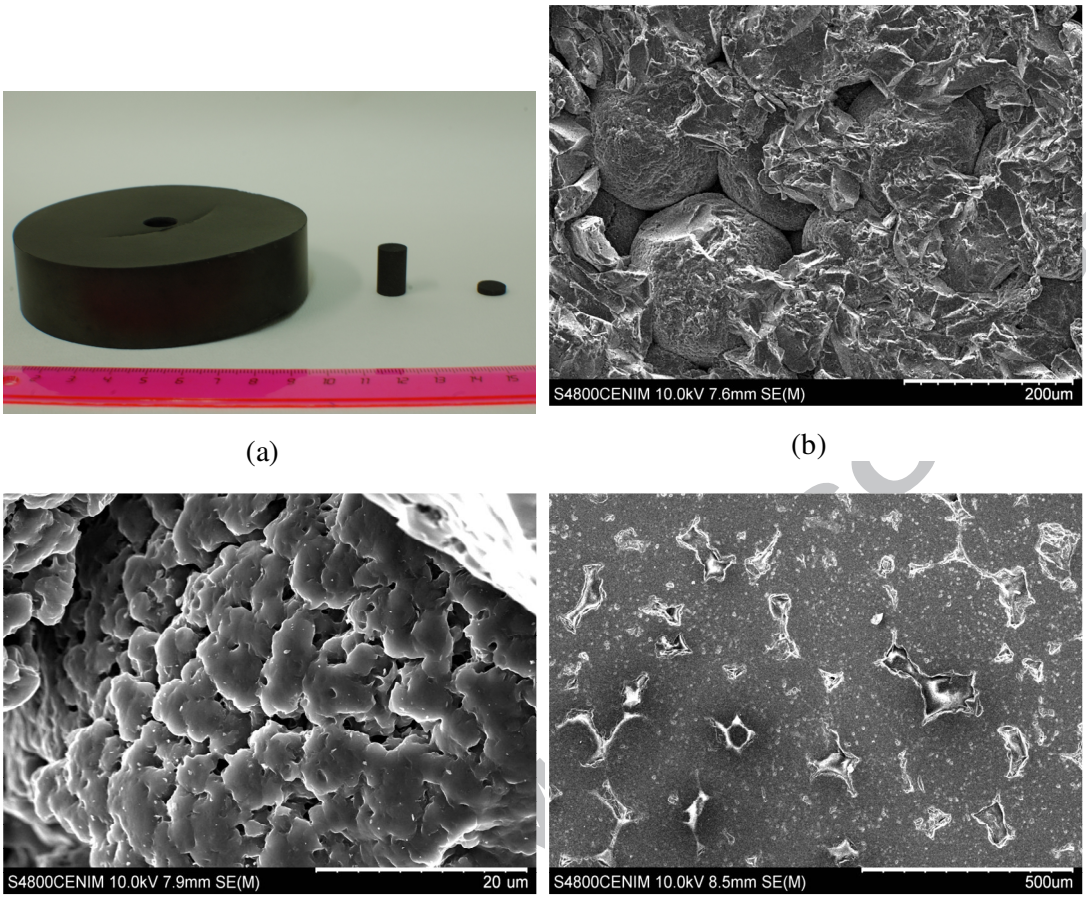

Fig. 1 - (a) Photograph, showing the large monolith fabricated by ATMI Co. (left), the smaller monolith extracted from it (middle), and the slizes used for electrochemical measurements (right). (b) SEM images, showing the carbon spheres forming the monolith, (c) the carbon particles forming the spheres, and (d) the connectivity between adjacent spheres. Voids between spheres and particles are also shown.

Table 1 compiles the density, electrical conductivity, and the CO, CO_2, and total O contents of the carbon monoliths (CM, CM-N_2, CM-Ar, CM-24 and CM-48). The CM monolith has a high density (1.17 g cm^{-3}), which agrees with the closely compacted microstructure. This high density, as it will be commented later on, is affected by the subsequent treatments carried out. The monolith density decreases slightly upon the inert heat-treatments (to 1.03 g cm^{-3} for CM-N_2 and to 1.07 g cm^{-3} for CM-Ar) and further upon the CO_2 activation (to 0.95 g cm^{-3} for CM-24, and to 0.80 g cm^{-3} for CM-48). Nevertheless, the density of these activated monoliths is much higher than the densities reported for other carbon monoliths (usually lower than 0.5 g cm^{-3}) [8,11,12-14,22-26,39,41,43] and for PVDC-based carbon powder pellets [45,46]. The good

Table 1 - Densities, electrical conductivities, as well as CO, CO_2, and total O contents (TPD) for all the monoliths.

	CM	CM-N_2	CM-24	CM-48	CM-Ar
Density, d (g cm^{-3})	1.17	1.03	0.95	0.80	1.07
Conductivity (S cm^{-1})	9.3	9.1	---	9.5	111
CO content (μmol g^{-1})	2411	1314	999	552	---
CO_2 content (μmol g^{-1})	955	657	442	196	---
O content (μmol g^{-1})	4320	2628	1883	915	---
O content, TPD (At.%)	6.91	4.21	3.01	1.46	---

connectivity between adjacent particles and adjacent spheres accounts for the high electrical conductivity of the carbon monoliths. The starting CM shows an electrical conductivity of 9.3 S cm^{-1}, which is among the highest values reported for carbon monoliths (mostly in the range of 1-10 S cm^{-1}) [11,23,39,41,43]. The electrical conductivity of the derived monoliths shows values (between 9.1 and 9.5 S cm^{-1}) as high as the starting CM within experimental error. It indicates that the heating at 1073 K in N_2 or in CO_2 do not affect either the individual carbon particles or the contacts between adjacent particles. Contrarily, the CM-Ar monolith shows, as expected, a much higher electrical conductivity (111 S cm^{-1}) due to the high temperature treatment used (2273 K) which causes a higher structural ordering degree.

Finally, Table 1 also presents the oxygen surface contents (*i.e.*, amounts of CO and CO_2 evolved during TPD) of all monoliths. It can be seen that CM has a considerable amount of surface oxygen groups. Upon thermal treatments in inert flows, the oxygen groups are significantly removed in N_2 (CM-N_2) and are totally eliminated in Ar (CM-Ar). Upon CO_2 activation, the oxygen contents of CM-24 and CM-48 further decrease in relation to CM-N_2. Such observation suggests that the CO_2 activation process preferentially removes reactive oxygenated carbon atoms, rather than creating stable oxygenated carbon atoms. This is evident considering that samples CM-24, and CM-48 did not have, as CM-N_2, a soaking time of 3 h in N_2 and that the decrease of surface oxygen groups increases with the activation time.

3.2. Textural characterization

The textural porosity of the starting CM monolith and the effects that the heat-treatments have on it can be seen in Table 2 and in Figure 2. The former outlines the porosity characteristics of the samples, *i.e.*, apparent surface areas and micropore volumes. The latter presents the adsorption isotherms of N_2 and CO_2, as well as the DFT pore size distributions (PSD).

The N_2 adsorption isotherm of the starting CM monolith shows a sharp increase in adsorption, followed by a knee and a plateau (see Figure 2a). It can be observed that most of the adsorption takes place at relative pressures below 0.1. The isotherm shape (type I according to the classification of the International Union of Pure and Applied Chemistry, IUPAC [47]), reveals the microporous structure of that monolith. The PSD (inset of Figure 2a) reveals that the porosity is due to micropores smaller than 1.1 nm with a significant amount of micropores smaller than 0.7 nm. This latter observation is confirmed by the similarity of the micropore volumes assessed from N_2 and CO_2 [48] (see Table 2). Also the N_2 adsorption isotherms of the derived monoliths CM-N_2, CM-24 and CM-48 are of type I. While CM-N_2 reaches the same adsorbed volume as CM,

Table 2 - Specific, and volumetric, BET surface areas, micropore volumes, gravimetric and volumetric capacitances.

	CM	CM-N_2	CM-24	CM-48	CM-Ar
S_{BET} (m^2g^{-1})	957	1030	1290	1684	2.9
S_{BET} (m^2cm^{-3})	1120	1061	1226	1347	3.1
$V_{DR}(N_2)$ (cm^3g^{-1})	0.382	0.415	0.517	0.674	0.001
$V_{DR}(CO_2)$ (cm^3g^{-1})	0.397	0.396	0.430	0.436	0.048
C_{1s} ($F\ g^{-1}$)	292	241	264	291	0
$C_{s,PS}$ ($F\ g^{-1}$)	152	83	63	35	0
$C_{s,DL}$ ($F\ g^{-1}$)	140	158	201	256	0
C_{1v} ($F\ cm^{-3}$)	342	248	251	232	0
$C_{v,PS}$ ($F\ cm^{-3}$)	178	85	60	28	0
$C_{v,DL}$ ($F\ cm^{-3}$)	164	163	191	205	0

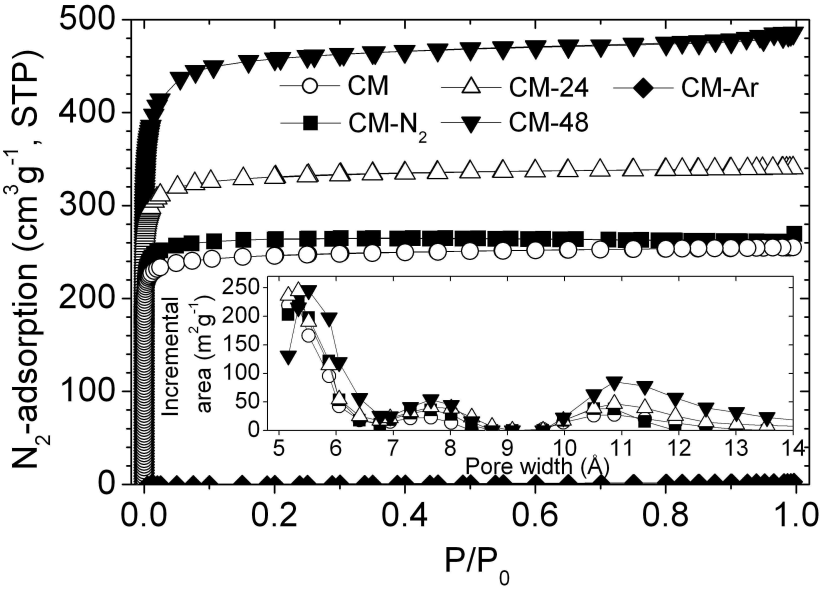

(a)

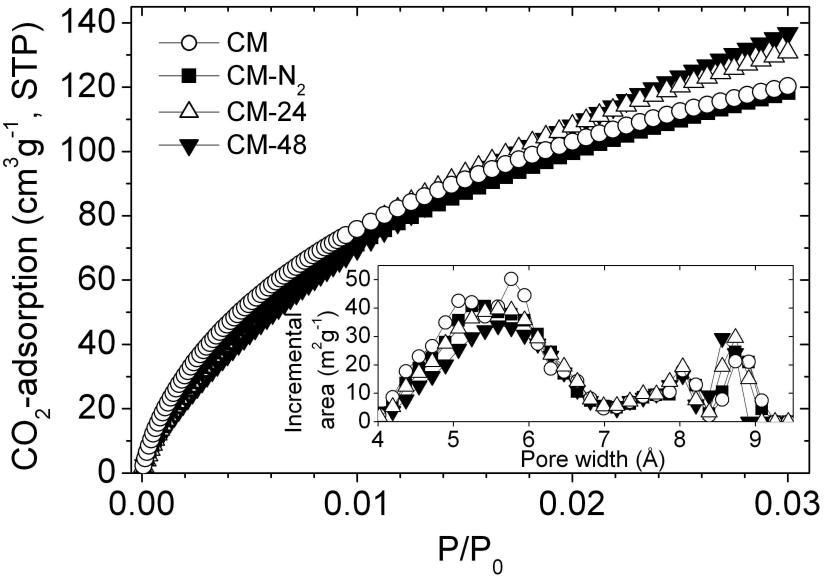

(b)

Fig. 2 - Adsorption isotherms of the monoliths studied with (a) N_2 at 77 K, and (b) CO_2 at 273 K. Insets: their DFT pore size distributions.

CM-24 and CM-48 show much higher adsorption capacities than CM, the adsorbed volume increasing as the activation time becomes longer. The N_2 adsorption isotherm of the CM-Ar monolith exhibits negligible adsorption capacity; its BET surface area is of 2.9 m^2 g^{-1}. Comparing the surface area and PSD of CM with those of CM-N_2, CM-24

and CM-48, the following observations can be made: i) there are no differences between CM and CM-N_2, pointing out similar porosity for these two samples, ii) in comparison with CM and CM-N_2, the activated monoliths CM-24 and CM-48 show larger surface areas and wider micropores, the latter as deduced from the slight shift of the peak at 1.1 nm. CO_2 adsorption isotherms and their corresponding PSDs (Figure 2b) confirm the important contribution of micropores with sizes smaller than 0.7 nm in the four monoliths.

These characteristics of the isotherms and PSD profiles are confirmed by the values reported in Table 2. Thus, the starting monolith CM shows a relatively large BET surface area of 957 m^2g^{-1} and micropore volumes $V_{DR}(N_2)$ and $V_{DR}(CO_2)$ of 0.38 and 0.40 cm^3g^{-1}, respectively. Upon heat-treatment in nitrogen (CM-N_2), the BET surface area and $V_{DR}(N_2)$ slightly increase, whereas $V_{DR}(CO_2)$ remains unaffected. The high temperature treatment in Ar (CM-Ar monolith) removed all the porosity. The heat-treatment followed by CO_2 activation (CM-24 and CM-48) causes a notable increase in porosity (BET surface area, $V_{DR}(N_2)$, and $V_{DR}(CO_2)$), which confirms the effectiveness of the CO_2 activation process. CM-48 reaches the highest BET surface area (1684 m^2g^{-1}) and micropore volumes ($V_{DR}(N_2)$ = 0.67 cm^3g^{-1} and $V_{DR}(CO_2)$ = 0.44 cm^3g^{-1}). It is important to note that for the monoliths studied in this paper, which have a well-defined microporous character, the term "specific surface area" should be understood as an apparent specific surface area, *i.e.*, using the Barrer´s concept [49].

3.3. Electrochemical characterization

From galvanostatic measurements in a symmetric two-electrode cell (2M aqueous solution of H_2SO_4), the electrochemical performances of the five monoliths were measured and are discussed in the following.

The specific capacitances or gravimetric capacitances (C_s), expressed in F g^{-1}, were determined according to $C_s=2\cdot I\cdot t_d/E_2\cdot m$, where I is the applied current, t_d is the discharge time, E_2 is the voltage decrease during the discharge, and m is the weight of one monolith in the cell (see inset of Figure 3a). The volumetric capacitances (C_v), *i.e.*, considering the electrode volume, are expressed in F cm^{-3} and were calculated according to $C_v=C_s\cdot d$, where d is the monolith density. Hence, C_s and C_v are referred to the monolith weight and volume, respectively.

The dependence of C_s as a function of the current density (j) is shown in Figure 3a for

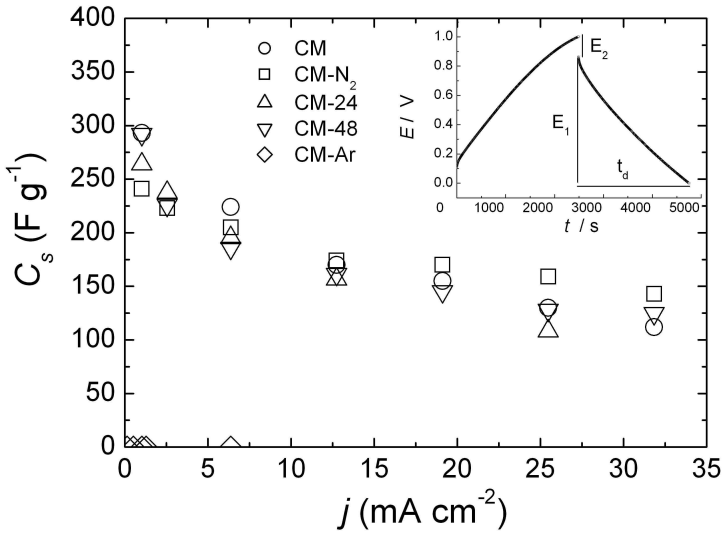

(a)

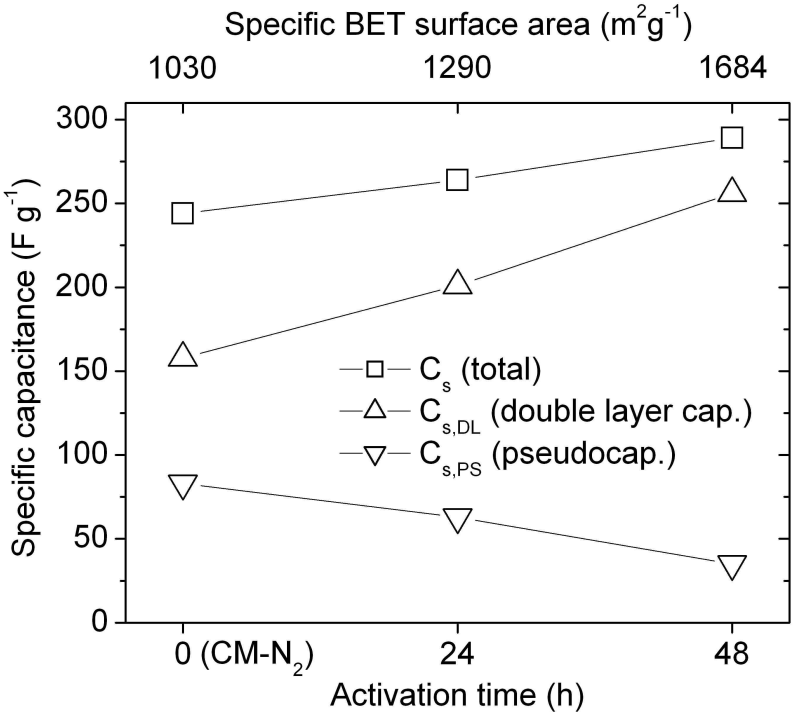

(b)

Fig. 3 - (a) Gravimetric capacitance *vs.* current density for the five monoliths and (b) gravimetric capacitances (total, pseudocapacitance and double layer capacitances) *vs.* activation time for CM-N_2, CM-24, and CM-48.

the five monoliths. At the low current density of 1 mA cm^{-2} (*i.e.,* in nearly steady conditions) the C_{1s} shows a value of 292 F g^{-1} for CM and values in the range 241-292 F g^{-1} for of the heat-treated monoliths (see Table 2). These values are higher than those reported for other carbon monoliths [4,8,9,11-14,22,23,40-43]. The monolith CM-Ar shows a negligible value of C_{1s} in accordance with its negligible surface area. Comparing the monoliths CM-N_2, CM-24 and CM-48 (Figure 3b), C_{1s} increases, as expected, with CO_2 activation time due to the increase of the adsorption capacities (*e.g.*, S_{BET} surface area), as it can be seen in the upper part of this figure. Curiously, as it will be discussed later on in Section 3.4, the starting monolith CM (not plotted in Figure 3b) presents, in relation to its S_{BET} surface area, a much higher C_{1s} (Table 2). In fact, although CM-48 has a much higher surface area than CM their C_{1s} shows the same values (291 and 292 F g^{-1}, respectively). In any case, it has to be noted that the C_{1s} values (between 241-292 F g^{-1}) are comparable to the highest values reported for other carbon electrodes [3,4,8,19,20,23,50-55] and are surprisingly high, considering that they are obtained in samples having relatively low surface areas (S_{BET} < 1700 m^2g^{-1}). At current densities above 1 mA cm^{-2}, C_s decreases as observed for other carbons. Because the monoliths studied in the present work have a thickness of 1.3-1.6 mm, a clear decrease of C_s is observed at higher current densities [40,41]. The decrease is associated with the presence of an equivalent series resistance (ESR) in the cell; this ESR increases as the monolith thickness does [41].

The volumetric capacitance (C_v) is plotted *vs.* current density for the five monoliths in Figure 4a. At 1 mA cm^{-2} current density, the C_{1v} shows values in the range of 232-342 F cm^{-3} for the monoliths CM, CM-N_2, CM-24 and CM-48, with a maximum value of 342 F cm^{-3} for CM. To the best of our knowledge, these volumetric capacitances are the highest reported for carbon electrodes at the time of writing [8,11,12,23, 40,45,52,53,57]. These exceptionally high C_{1v} values are due to a suitable combination of high C_s and high density (C_v=C_s·d). The monolith CM-Ar shows a negligible C_{1v} in agreement with its negligible C_{1s}. At current densities above 1 mA cm^{-2}, C_v decreases in a parallel way to that observed for C_s and already discussed.

The effect that the activation time of the heat-treated monoliths has on their C_{1v} values (CM-N_2, CM-24, and CM-48) can be observed in Figure 4b. Unlike the C_{1s} variation in Figure 3b, C_{1v} remains constant from 0 h to 24 h, around 250 F cm^{-3} and drops to 232 F cm^{-3} for an activation time of 48 h. Such variation with the time of activation cannot be explained by the decrease of the density (from 1.03 g cm^{-3} for CM-N_2 to 0.80 g cm^{-3} for

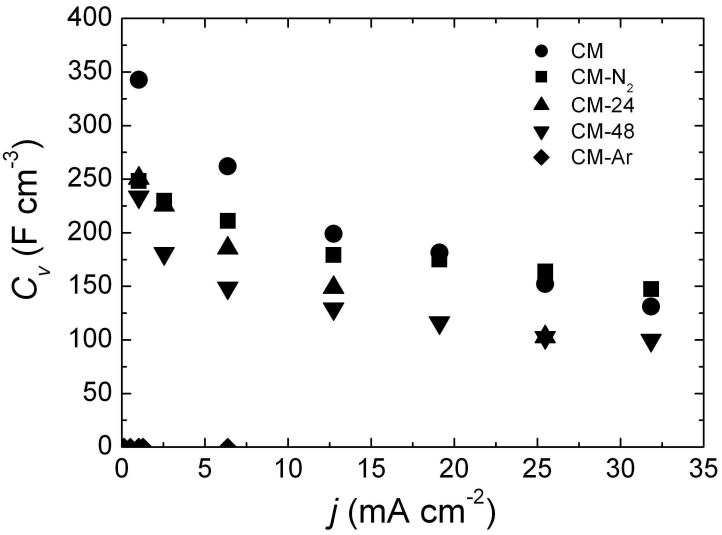

(a)

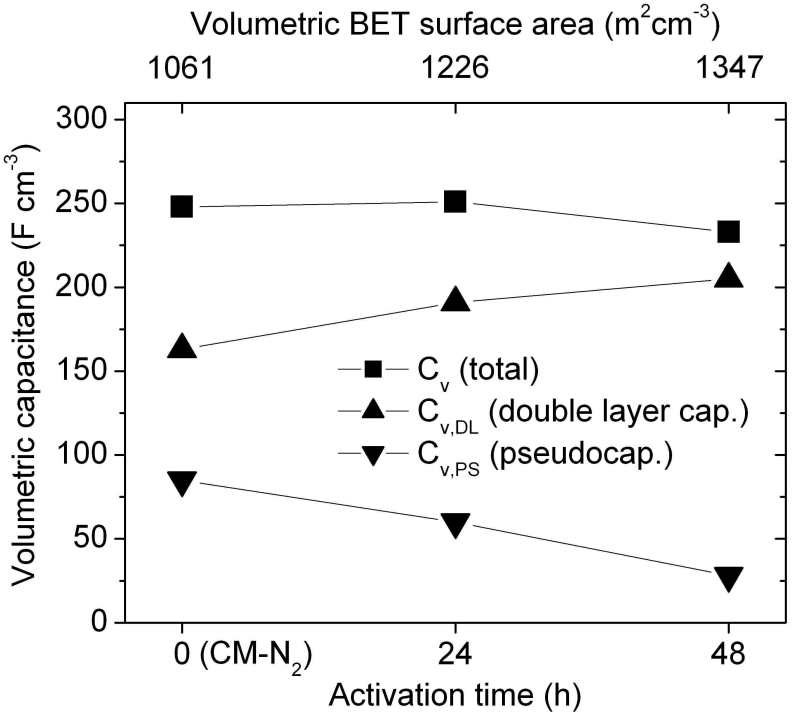

(b)

Fig. 4 - (a) Volumetric capacitance *vs.* current density for the five monoliths and (b) volumetric capacitances (total, pseudocapacitance, and double layer capacitances) *vs.* activation time for CM-N_2, CM-24, and CM-48.

CM-48; *i.e.,* the decrease being of 22 %) because there is also a subsequent increase of the apparent S_{BET} surface area (from 1030 m^2 g^{-1} of CM-N_2 to 1684 m^2g^{-1} of CM-48; *i.e.,* the increase being of 63%). In fact, the surface area of the monoliths expressed per unit of volume ($S_{BET\ v}=S_{BET}\cdot d$) increases with the time of activation from 1061 m^2 cm^{-3} for CM-N_2 to 1347 m^2 cm^{-3} for CM-48 (see Table 2 and Figure 4b). Therefore, the trend found for C_{1v} in Figure 4b suggests, as it will be discussed in Section 3.4, that another variable (*i.e.*, the pseudocapacitance) affects the C_{1v} values.

Energy densities, referred to the monolith weight (W_s) and monolith volume (W_v), were calculated according to $W_s=(1/2)\cdot C_s\cdot E_2^2$ and $W_v=(1/2)\cdot C_v\cdot E_2^2$, respectively, where C_s, C_v and E_2 were measured at each current density. E_2 is the voltage decrease during the discharge as shown in inset of Figure 4a. Power densities referred to the monolith weight (P_s) and monolith volume (P_v) were calculated according to $P_s=W_s/t_d$ and $P_v=W_v/t_d$, respectively, where t_d is the discharge time measured at each current density. The Ragone plots of P_s *vs.* W_s and P_v *vs.* W_v are shown in Figures 5a and 5b, respectively. It can be seen that CM, CM-N_2, CM-24, and CM-48 reach energy densities as high as 38 Wh kg^{-1} and 44 Wh L^{-1}, and power densities as high as 176 W kg^{-1} and 183 W L^{-1}. The power and energy density values for the starting monolith CM reach the highest edge values. However, the heat-treated monolith performs better in the intermediate range, with better ratio between power and energy density. In comparison with results reported for other carbon monoliths in acidic electrolyte [8,11,56], our monoliths show higher gravimetric and volumetric energy densities, due to their higher gravimetric C_s and C_v values. However, our gravimetric power densities are lower probably associated with higher ESR of the cell, the latter being affected not only by the monolith thickness but also by the monolith/collector resistance. The gravimetric power density of our monoliths could be increased if the monolith thickness would be decreased to 100-150 µm and the monolith/collector resistance would be lower [40]. If the gravimetric power density is calculated according to $P=V^2/4\cdot ESR\cdot m$, where V= 1 V and m is the weight of one monolith, the values obtained are 146, 393, 148 and 359 W $kg^{-1}$for the monoliths CM, CM-N_2, CM-24, and CM-48, respectively.

Cycle life was studied at 31 mA cm^{-2} on the starting monolith CM. This monolith was chosen because it shows the highest content in surface oxygen groups, as deduced from TPD, hence, it is the most sensible on cycling. Interestingly, after 10,000 charge/discharge cycles the capacitance retention was 97%.

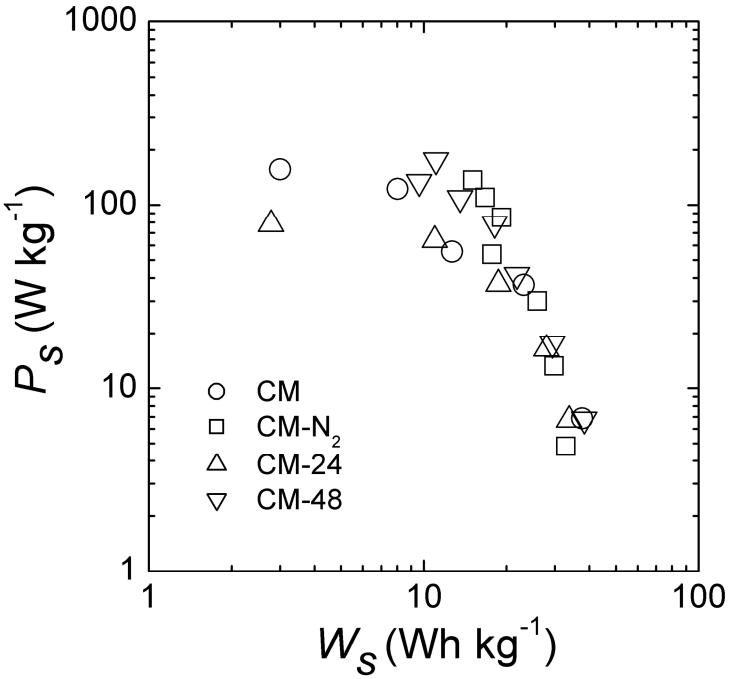

(a)

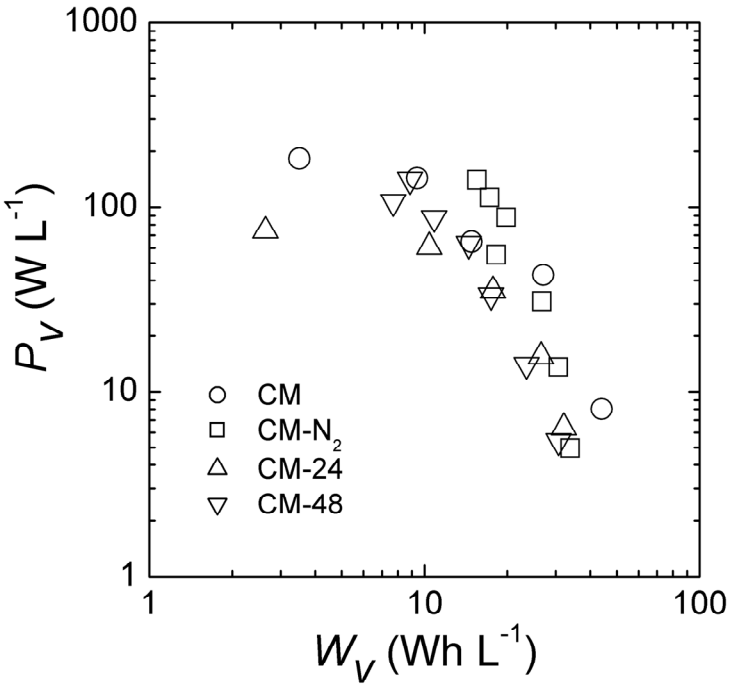

(b)

Fig. 5 - Ragone plots with power density *vs.* energy density, referred to the mass (a), and the volume (b) of the monoliths.

3.4. Further look to the capacitance results: pseudocapacitance contribution

The two apparently conflicting results that have been noted previously are discussed next. These are: i) The C_{1s} values of monoliths CM (292 F g^{-1}) and CM-48 (291 F g^{-1}) are the same, whereas their S_{BET} surface areas are quite different (957 m^2g^{-1} and 1684 m^2g^{-1}, respectively), and ii) the different trends found for C_{1s} and C_{1v} *versus* activation time for samples CM-N_2, CM-24, and CM-48: C_{1s} increasing with the activation time (Figure 3b), whereas C_{1v} slightly decreasing (Figure 4b).

Carbon materials can have various types of functional groups on their surface (*e.g.*, –COOH, –CO, and others). Some of them are basic and can undergo the well-known mechanism for the quinone/hydroquinone redox pair. Hence, they are electrochemically active, increasing the total capacitance by the contribution of a pseudocapacitance through faradic reactions of these groups with the electrolyte ions (*e.g.*, CO-type surface complexes) [57,58]. The contribution of these CO-generating oxygen groups to the capacitance has been suggested in early publications [59-61] and has been well established in further works [62,63]. The results found in the latter works, using a large series of KOH-activated carbons, show that the CO-type oxygen groups have a positive contribution to the capacitance [62,63]. A very good correlation between the specific capacitance and this type of oxygen groups has been found [62,63]. Later on, and based on these results, attempts to analyze the pseudocapacitance contribution have been reported [64].

In relation to the former point i), the unique difference between CM and CM-48 is their different CO and CO_2 contents and their different oxygen contents (Table 1), which are much higher for CM than for CM-48. Such higher content in oxygen functionalities can explain the unexpected higher C_{1s} value of CM, in relation to CM-48. The presence of those oxygen groups can induce reversible redox reactions with protons of the electrolyte, and, consequently, they can add pseudocapacitance contributions to the double layer capacitance of both C_{1s} and to C_{1v}.

We can expect that:

$$C_{1s} = C_{sDL} + C_{sPS}$$

where C_{1s} is the gravimetric capacitance (measured at 1 mA cm^{-2}), C_{sDL} is the double layer capacitance due to the formation of the double layer between the electrolyte ions and the carbon surface, and C_{sPS} is the pseudocapacitance due to the reversible redox reactions that occur between the electrolyte ions and oxygen groups at the surface of the

carbon particles. Because C_{sDL} and C_{sPS} come from two different phenomena they appear as parallel processes, and, hence, the total capacitance is the summation of the two capacitances, C_{sDL} and C_{sPS} [64-68].

To separate the contribution of the pseudocapacitance from that of the double-layer is not a simple task, because, among other, the different oxygen groups (ketone, carboxylic acid, anhydrides, etc.) can contribute to the pseudocapacitance and their contribution could be different. In fact, papers dealing with such separation are very scarce [69] and only recently a suitable attempt has been proposed, based on the linear relationship existing between pseudocapacitance and content of CO-generating oxygen groups [64,67].

The presence of pseudocapacitance in the CM monolith is confirmed from the cyclic voltammetry obtained in the three-electrode cell (Figure 6). Broad peaks at ca. -0.15 V in charge and ca. -0.25 V in discharge evidence a pseudocapacitive contribution in addition to the double layer capacitance. The broad peaks are also observed for the monolith CM-48, but they are less intense. This is in agreement with the lower content of oxygenated groups in this monolith (Table 1).

Taking into account that the monoliths studied in the present paper are mainly microporous (with negligible amounts of larger pores), the pseudocapacitance contribution and, hence, the double layer capacitance contribution, have been assessed

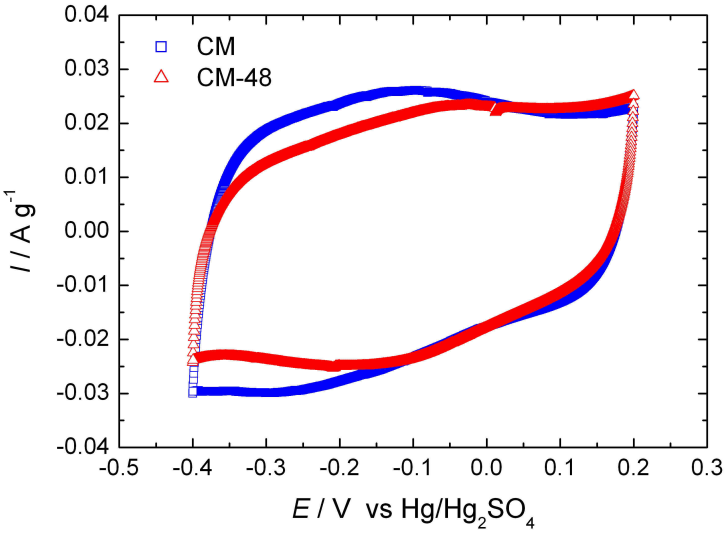

Fig. 6 - Cyclic voltammetries obtained with a three-electrode cell for the monoliths CM and CM-48. The voltage scan rate was 0.1 mV s^{-1} in the two cases.

following the methodology described for microporous carbons elsewhere [64,67]. In these works, the pseudocapacitance was found to depend linearly on the content of CO-evolving groups according to the rate 0.063±0.005 F μmol^{-1} of CO for microbead activated carbons [64] and according to 0.042±0.008 F μmol^{-1} of CO for activated carbon nanofibers [67]. These values are close within experimental error. Because the carbon monoliths investigated in this work are made from connected bead particles of carbon, the value of 0.063±0.005 F μmol^{-1} of CO was chosen to estimate the pseudocapacitance. Thus, the C_{sPS} of each monolith was estimated by multiplying 0.063 F·μmol^{-1} of CO into the CO content (Table 1). Then, subtracting C_{sPS} from C_{1s} gave C_{sDL} for each monolith (Table 2). It is worth to note that the C_{1s} value of CM and CM-48 are the same, because their different contributions of C_{sDL} and C_{sPS} are compensated. CM shows a significantly higher C_{sPS} value, due to its higher oxygen content. However, CM-48 reveals a dominant C_{sDL} value, due to its large apparent surface area (Table 2).

In relation to point ii), Figure 3b compares the values of gravimetric C_{sDL} and C_{sPS} with those of total C_{1s}. In a parallel way, Figure 4b compares the values of volumetric C_{vDL} and C_{vPS} with those of total C_{1v}. In the two figures, C_{sDL} and C_{vDL} increase as the activation time becomes longer, being in agreement with the increase of the BET surface areas. In the two figures, C_{sPS} and C_{vPS} decrease as the activation time becomes longer. These trends are consistent with the progressive decrease of the content of surface oxygen groups (see Table 1). For the gravimetric capacitances, the increase of C_{sDL} dominates the decrease of C_{sPS} and, hence, the total C_{1s} increases with activation time. For the volumetric capacitances, the decrease of C_{vPS} dominates the increase of C_{vDL}, hence, the total C_{1v} decreases on activation time. The different trends found for the total C_{1s} and C_{1v} values in Figures 3b and 5b can be explained by the different contributions of their double layer capacitance and pseudocapacitance, solving the above noted discrepancies concerning the different trends of C_{1s} and C_{1v} *versus* activation time.

The dependence of the gravimetric and volumetric capacitances as a function of the apparent BET surface area is shown in Figure 7 for the five monoliths studied. The gravimetric C_{sDL} follows a good linear correlation with S_{BET}, having a correlation factor of 0.99993 (Figure 7a). Similar linear dependences are also obtained if other apparent specific surface areas are taken, *e.g.*, S_{DR}, S_{DFT}, $S_{t\text{-}plot}$, etc. (see Table 3). Contrarily, in Figure 7a the gravimetric C_{sPS} shows no correlation with S_{BET} (neither with the other surface areas), because that magnitude only depends on the content of surface oxygen

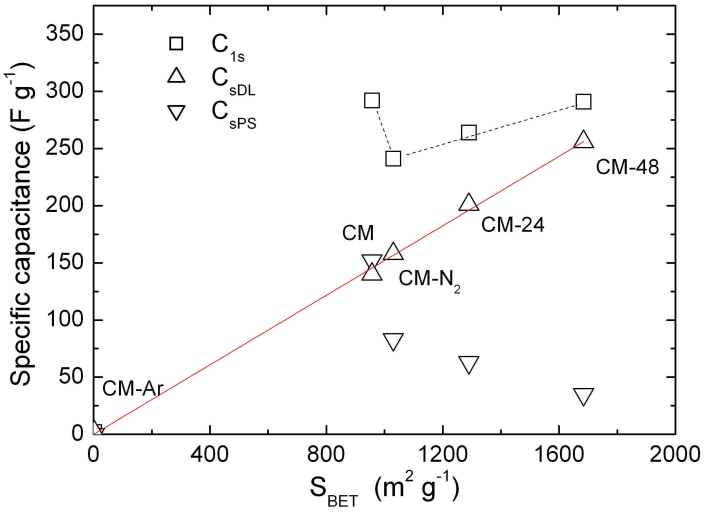

(a)

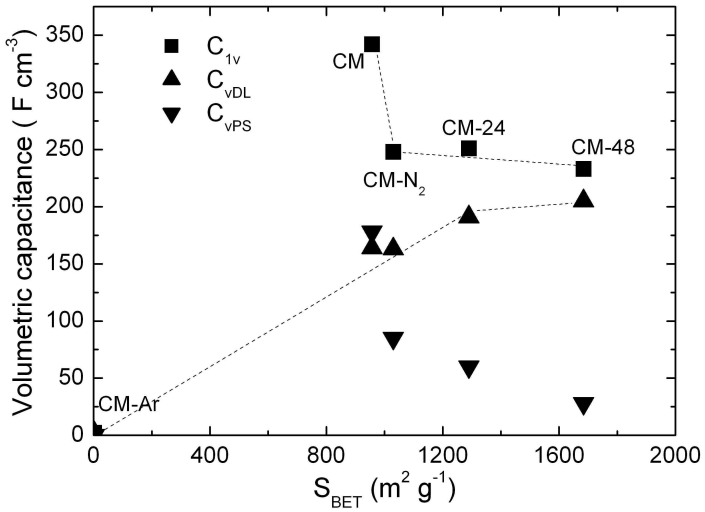

(b)

Fig. 7 - Gravimetric capacitance (a) and volumetric capacitance (b) *vs.* apparent BET surface area.

groups, as already discussed. As a result the total gravimetric capacitance ($C_{1s} = C_{sDL} + C_{sPS}$) shows no linear correlation with S_{BET} (neither with other surface areas).

Regarding the volumetric capacitances, the correlation of C_{1v}, C_{vDL} and C_{vPS} with S_{BET} is shown in Figure 7b. C_{vDL} shows a linear dependence with a lower correlation factor (0.98) for the monoliths CM-Ar, CM, CM-N_2 and CM-24. However, CM-48

Table 3 - Apparent surface areas from the N_2 and CO_2 adsorption isotherms for all the monoliths: CM, CM-N_2, CM-24 and CM-48.

Surface area (m^2g^{-1})	**CM**	**CM-N_2**	**CM-24**	**CM-48**
N_2-S_{BET}	957	1030	1290	1684
N_2-S_{DR}	1075	1166	1454	1896
N_2-$S_{\alpha\text{-plot}}$ *	899	914	1053	1116
N_2-$S_{t\text{-plot}}$	832	839	1151	1452
N_2-S_{DFT} < 2nm	966	1067	1262	1625
CO_2-S_{DR}	991	989	1072	1088
CO_2-S_{DFT} < 2nm	912	910	1025	1114

* Using as reference the CM sample treated up to 2273 K in Ar (CM-Ar)

departs from such linear dependence. The fact that C_{vDL} is affected by both, S_{BET} and the monolith density, explains this observation. When the variation of the monolith density is important, the correlation of C_{vDL} varies in line with the available volumetric surface area (S_{BET}, m^2cm^{-3}; Table 2), not with the specific S_{BET}. Interestingly, because C_{vPS} depends mainly on the content of surface oxygen groups it does not depend on S_{BET}, although obviously it affects C_{1v}, which also shows no correlation with S_{BET}.

4. Conclusions

The monoliths studied in this work show a network of connected carbon particles and voids. The closely compacted structure accounts for the high density and the high electrical conductivity of the monoliths. The content of surface oxygen functionalities is higher for the starting monolith than for the monolith heat-treated in N_2, and further decreases upon CO_2 activation as the activation time becomes longer.

The singular characteristics of these monoliths make them suitable electrodes for supercapacitors. Their performance in sulfuric acid medium shows high specific capacitances (as high as 292 F g^{-1}), which can be obtained either from a significant contribution of pseudocapacitance in the starting monolith, or from a dominant contribution of the double layer capacitance upon CO_2 activation. Exceptionally high volumetric capacitances (as high as 342 F cm^{-3}) are reached due to the high specific

capacitance and the high density of the monoliths. Furthermore, high gravimetric energy and power densities (38 Wh kg^{-1} and 176 W kg^{-1}, respectively), and high volumetric energy and power densities (44 Wh L^{-1} and 183 W L^{-1}, respectively) are obtained. The exceptionally good performances of the monoliths (on both, gravimetric and volumetric basis) can be related to i) their very dense structures, showing a good connectivity of the carbon particles and a high electrical conductivity, and ii) suitable porosities and surface oxygen contents which optimize the interaction between the carbon surface and the electrolyte ions.

Acknowledgements

The authors would like to thank A.B. García-Suarez (from INCAR, Oviedo, Spain) for performing the heat-treatment in Ar. Financial support from projects MAT2011-25198, MP1004 and PROMETEO/2009/047 is gratefully acknowledged. V.B. thanks MINECO for R&C contract.

References

[1] Simon P, Gogotsi Y. Nature Mater 2008; 7:845-54.

[2] Miller JR, Simon P. Science 2008; 321:651-2.

[3] Department of Energy (DOE), Basic research needs for electrical energy storage, online, 2007.

[4] Liu C, Li F, Ma LP, Cheng HM. Adv Mater 2010; 22:E28-E62.

[5] Conway BE. Electrochemical Supercapacitors: Scientific Fundamentals and Technological Applications. New York: Kluwer; 1999.

[6] Yang H, Shi Q, Liu X, Xie S, Jiang D, Zhang F, et al. Chem Commun 2002; 2842-3.

[7] Taguchi A, Smatt JH, Linden M. Adv Mater 2003; 15:1209-11.

[8] Ruiz V, Blanco C, Santamaria R, Ramos-Fernandez JM, Martinez-Escandell M, Sepulveda-Escribano A, et al. Carbon 2009; 47:195-200.

[9] Bruno MM, Cotella NG, Miras MC, Barbero CA. Colloids Surfaces A: Physicochem Eng Aspects 2010; 362:28-32.

[10] Garcia-Gomez A, Miles P, Centeno TA, Rojo JM. Electrochem Solid-State Lett 2010; 13:A112-A114.

[11] Taer E, Deraman M, Talib IA, Awitdrus A, Hashmi SA, Umar AA. Int J Electrochem Sci 2011; 6:3301-15.
[12] Awitdrus A, Deraman M, Talib IA, Farma R, Omar R, Ishak MM, et al. Adv Mater Research 2012; 501:13-8.
[13] Liu MC, Kong LB, Zhang P, Luo YC, Kang L. Electrochim Acta 2012; 60:443-8.
[14] Goodman PA, Li H, Gao Y, Lu YF, Stenger-Smith JD, Redepenning J. Carbon 2013; 55:291-8.
[15] Sevilla M, Fuertes AB. Carbon 2013; 56:155-66.
[16] Saliger R, Fischer U, Herta C, Fricke J. J Non-Cryst Solids 1998; 225:81-5.
[17] Batalla Garcia B, Feaver AM, Zhang Q, Champion RD, Cao G, Fister TT, et al. J App Phys 2008; 104:014305.
[18] Halama A, Szubzda B, Pasciak G. Electrochim Acta 2010; 55:7501-5.
[19] Zhao L, Fan LZ, Zhou MQ, Guan H, Qiao S, Antonietti M, et al. Adv Mater 2010; 22:5202-6.
[20] Béguin F, Frackowiak E. Carbons for Electrochemical Energy Storage and Conversion Systems. Boca Raton FL: CRC Press; 2010.
[21] Gogotsi Y, Simon P. Science 2011; 334:917-8.
[22] Wu D, Fu R, Zhang S, Dresselhaus M, Dresselhaus G. Carbon 2004; 42:2033-9.
[23] Carriazo D, Pico F, Gutierrez MC, Rubio F, Rojo JM, del Monte F. J Mater Chem 2010; 20:773-80.
[24] Biener J, Stadermann M, Suss M, Worsley MA, Biener MM, Rose KA, et al. Energy Environ Sci 2011; 5:656-67.
[25] Brun N, Prabaharan SRS, Surcin C, Morcrette M, Deleuze H, Birot M, et al. J Phys Chem C 2012; 116:1408-21.
[26] Candelaria SL, Chen R, Jeong YH, Cao G. Energy Environ Sci 2012; 5:5619-37.
[27] Lozano-Castello D, Cazorla-Amorós D, Linares-Solano A, Quinn DF. Carbon 2002; 40:2817-25.
[28] Marco-Lozar JP, Kunowsky M, Suárez-García F, Carruthers JD, Linares-Solano A. Energy Environ Sci 2012; 5:9833-42.
[29] Arno J, Carruthers D, Sturm E, Wang L, Olander K, Van Buskirk P. Gases and Technology 2005; 4.
[30] Linares-Solano A, Cazorla-Amorós D, Marco-Lozar JP, Suárez-García F. In: Ortiz OL, Ramírez LD, editors. Coordination Polymers and Metal Organic Frameworks, New York: Nova Science Publishers Inc.; 2011, p. 197-224.

[31] Yu JS, Kang S, Yoon SB, Chai G. J Am Chem Soc 2002; 124:9382-3.
[32] Baumann TF, Satcher Jr JH. J Non-Cryst Solids 2004; 350:120-5.
[33] Mukai SR, Nishihara H, Yoshida T, Taniguchi K, Tamon H. Carbon 2005; 43:1563-5.
[34] Tonanon N, Siyasukh A, Wareenin Y, Charinpanitkul T, Nishihara H, Mukai SR, et al. Carbon 2005; 43:2808-11.
[35] Zhou Z, Yan Q, Su F, Zhao XS. J Mater Chem 2005; 15:2569-74.
[36] Liu N, Zhang S, Fu R, Dresselhaus MS, Dresselhaus G. J Appl Polymer Sci 2007; 104:2849-55.
[37] Li J, Wang X, Wang Y, Huang Q, Dai C, Gamboa S, et al. J Non-Cryst Solids 2008; 354:19-24.
[38] Xu S, Li J, Qiao G, Wang H, Lu T. Carbon 2009; 47:2103-11.
[39] Kim SJ, Hwang SW, Hyun SH. J Mater Sci 2005; 40:725-31.
[40] Chmiola J, Celine Largeot PLT, Simon P, Gogotsi Y. Science 2010; 328:480-3.
[41] Garcia-Gomez A, Miles P, Centeno TA, Rojo JM. Electrochim Acta 2010; 55:8539-44.
[42] Staiti P, Arenillas A, Lufrano F, Menendez JA. J Power Sources 2012; 214:137-41.
[43] Zeller M, Lorrmann V, Reichenauer G, Wiener M, Pflaum J. Adv Energy Mater 2012; 2:598-605.
[44] US patent 6743278, 2004.
[45] Xu B, Wu F, Chen S, Zhou Z, Cao G, Yang Y. Electrochim Acta 2009; 54:2185-9.
[46] Endo M, Kim YJ, Takeda T, Maeda T, Hayashi T, Koshiba K, et al. J Electrochem Soc 2001; 148:A1135-A1140.
[47] Sing KSW, Everett DH, Haul RAW, Moscou L, Pierotti RA, Rouquerol J, et al. Pure Appl Chem 1985; 57:603-19.
[48] Cazorla-Amorós D, Alcaniz-Monge J, Linares-Solano A. Langmuir 1996; 12:2820-4.
[49] Barrer RM. In: Everett DH, Stone FS, editors. Structure and properties of porous materials. London: Butterworths; 1958, p. 50.
[50] Raymundo-Piñero E, Kierzek K, Machnikowski J, Béguin F. Carbon 2006; 44:2498-507.
[51] Pan H, Poh CK, Feng YP, Lin J. Chem Mater 2007; 19:6120-5.

[52] Zhang H, Cao G, Wang Z, Yang Y, Shi Z, Gu Z. Nano Lett 2008; 8:2664-8.
[53] Zhang H, Cao G, Yang Y, Gu ZJ. J Electrochem Soc 2008; 155:K19-K22.
[54] Fan Z, Yan J, Zhi L, Zhang Q, Wei T, Feng J, et al. Adv Mater 2010; 22:3723-8.
[55] Zheng C, Qian W, Weih F. Mater Sci Eng B 2012; 177:1138-43.
[56] Carriazo D, Gutierrez MC, Pico F, Rojo JM, Fierro JLG, Ferrer ML, et al. ChemSusChem 2012; 5:1405-9.
[57] Conway BE, Birss V, Wojtowicz J. J Power Sources 1997; 66:1-14.
[58] Qu D. J Power Sources 2002; 109:403-11.
[59] Hsieh CT, Teng H. Carbon 2002; 40:667-74.
[60] Nian YR, Teng H. J Electroanal Chem 2003; 540:119-27.
[61] Okajima K, Ohta K, Sudoh M. Electrochim Acta 2005; 50:2227-31.
[62] Bleda-Martínez MJ, Maciá-Agulló JA, Lozano-Castelló D, Morallón E, Cazorla-Amorós D, Linares-Solano A. Carbon 2005; 43:2677-84.
[63] Bleda-Martínez MJ, Lozano-Castelló D, Morallón E, Cazorla-Amorós D, Linares-Solano A. Carbon 2006; 44:2642-51.
[64] Centeno TA, Hahn M, Fernandez J, Kotz R, Stoeckli F. Electrochem Comun 2007; 9:1242-6.
[65] Nian YR, Teng H. J Electrochem Soc 2002; 149:A1008-A1014.
[66] Hu CC, Su JH, Wen TC. J Phys Chem Solids 2007; 68:2353-62.
[67] Barranco V, Lillo-Rodenas MA, Linares-Solano A, Oya A, Pico F, Ibañez J, et al. J Phys Chem C 2010; 114:10302-7.
[68] Inagaki M, Konno H, Tanaike O. J Power Sources 2010; 195:7880-903.
[69] Raymundo-Piñero E, Leroux F, Beguin F. Adv Mater 2006; 18:1877-82.